Astronomy & Astrophysics

Simulations of polarized dust emission

V.-M. Pelkonen[1], M. Juvela[1], and P. Padoan[2]

[1] Observatory, University of Helsinki, Tähtitorninmäki, PO Box 14, 00014 University of Helsinki, Finland
e-mail: vpelkone@astro.helsinki.fi; mika.juvela@helsinki.fi
[2] Department of Physics, University of California, San Diego, CASS/UCSD 0424, 9500 Gilman Drive, La Jolla, CA 92093-0424, USA
e-mail: ppadoan@ucsd.edu

ABSTRACT

Aims. The aim is to study the polarization of thermal dust emission to see if the alignment of the grain by radiative torques could explain the observed relation between the degree of polarization and intensity. Predictions are made for polarimetry observations with the Planck satellite.

Methods. Our results are based on model clouds derived from MHD simulations of magnetized turbulent flows. The continuum radiative transfer problem is solved with Monte Carlo methods to estimate the three-dimensional distribution of dust emission and the radiation field strength affecting the grain alignment. The minimum grain size aligned by the radiative torques is calculated, and the Rayleigh polarization reduction factor, R, is derived for different grain size distributions. We show maps of polarized thermal dust emission that are predicted by the models. The relation between the intensity and polarization degree is examined in self-gravitating cores. Furthermore, we study the effects of wavelength, resolution, and observational noise.

Results. We are able to reproduce the P/I-relation with the grain alignment by radiative torques. The decrease in intrinsic polarization and total emission means that sub-mm polarimetry carries only a little information about the magnetic fields in dense cores with high visual extinction. The interpretation of the observations will be further complicated by the unknown magnetic field geometry and the fact that what is observed as cores may, in fact, be a superposition of several density enhancements. According to our calculations, Planck will be able to map dust polarization reliably when A_V exceeds $\sim 2^m$ at spatial resolution of $\sim 15'$.

Key words. dust, extinction – ISM: clouds – polarization – radiative transfer

1. Introduction

Magnetic fields play an important role in the dynamics of molecular clouds and in the star formation process. In protostellar cores the topology of the magnetic fields can be predicted with models of core formation and evolution. However, observations of the magnetic field structure are needed to test such models. The best technique for studying magnetic fields in molecular clouds is to observe the polarization of the light from background stars and the polarization of the thermal dust emission, both arising because dust grains are aligned by the magnetic field.

Although the polarization of starlight by aligned interstellar dust grains was discovered over half a century ago (Hall 1949; Hiltner 1949), the processes responsible for the alignment are still under study. In a recent review by Lazarian (2003) the various proposed mechanisms are discussed extensively. One of the first processes to be suggested was the paramagnetic mechanism (Davis & Greenstein 1951), which is based on direct interaction of rotating grains with the interstellar magnetic field. While this mechanism requires stronger magnetic fields than have been uncovered by other means, it may contribute at very small grain sizes. Purcell (1979) introduced several processes to make grains very fast "suprathermal" rotators and identified one of them, catalytic sites ejecting H$_2$, as the major cause of fast grain rotation. However, it could not explain, for example, why the observations indicated that small grains are less aligned than large ones. Fairly recently, the Purcell mechanism was re-evaluated in a series of papers by Lazarian and colleagues, pointing out

processes such as internal grain wobbling (e.g., Jones & Spitzer 1967; Lazarian 1994; Lazarian & Roberge 1997), grain flipping (Lazarian & Draine 1999a), and "nuclear relaxation" (Lazarian & Draine 1999b). All these contribute to making the Purcell mechanism inefficient.

The radiative torque mechanism was introduced by Dolginov (1972) and Dolginov & Mytrophanov (1976). Draine & Weingartner (1996) demonstrated the efficiency of radiative torques using numerical simulations, while Abbas et al. (2004) demonstrated it in a laboratory setup. The radiative torque mechanism means the transfer of momentum by collisions of photons onto the grain, causing a torque which makes the grain rotate around its axis. The predictions of the radiative torque mechanisms are roughly consistent with observations (e.g., Lazarian et al. 1997; Hildebrand et al. 2000). In view of this, the radiative torque mechanism is a strong candidate as the primary mechanism for grain alignment inside molecular clouds. Cho & Lazarian (2005) showed that even deep inside GMCs ($A_V \leq 10$), large grains can be aligned by radiative torques, using a simple, radially symmetric core model. Thus, far-infrared and submillimeter polarimetry could reliably reflect the structure of magnetic fields deep inside molecular clouds.

Padoan et al. (2001) used numerical MHD simulations to model a molecular cloud containing protostellar cores, and computed dust continuum polarization for self-gravitating cores. They made the simplifying assumption that the temperature of the dust is uniform, which allowed them to calculate the polarization based on gas density and magnetic field vectors. They calculated the polarization maps for two cases: one where the

grain alignment mechanism efficiency would be independent of the visual extinction, and another where it was assumed that the mechanism would stop working at a sharp cut-off of $A_V = 3^m$, and thus dense cores would not contribute to the polarization. The latter case reproduced the observed results of decreasing polarization degree with increasing intensity in the cores, which led them to conclude that the grains at high visual extinction appear not to be aligned. This would mean that submillimeter polarization maps carry little information on the magnetic fields inside protostellar cores at visual extinction larger than $A_V \approx 3^m$.

Like Padoan et al. (2001), we base our study on three-dimensional simulations of magnetized gas flow, but we refine the analysis method used to predict the polarized dust emission. Radiative transfer calculations are used to estimate the actual three-dimensional distribution of dust emission. This naturally reduces the weight of high column density regions because the emission there will be reduced by the attenuation of the heating radiation field. Similarly, radiative transfer modeling allows us to estimate, at every point of the cloud, the radiative torque efficiency of Cho & Lazarian (2005). This way we can test the hypothesis that the reduced polarization of dense cores could be due to the non-alignment of smaller grains. We study the general morphology of the resulting dust polarization maps. In particular, we look at the relation between total and polarized dust emission in dense cores. Finally, some predictions are made concerning the dust polarization that will be observable with the Planck satellite.

2. Polarization

2.1. Rayleigh polarization reduction factor

The Rayleigh polarization reduction factor R is a measure of imperfect alignment of the dust grains with respect to the magnetic field (Greenberg 1968; see also Lee & Draine 1985). The degree of polarization is decreased when part of the grains are misaligned with respect to the magnetic field. In our case, small grains are not aligned by radiative torques, while the larger ones are. Cho and Lazarian (2005) give a fitting formula for the minimum aligned grain size in the case of a spherically symmetric dark cloud:

$$a_{\text{alg}} = (\log n_{\text{H}})^3 (A_{V,1D} + 5)/2800 \, \mu m, \tag{1}$$

where n_{H} is the hydrogen density and $A_{V,1D}$ is the visual extinction used by Cho & Lazarian (2005). They used the radiation field given in Mathis et al. (1983), which was given as a function of the visual extinction measured along a perpendicular sight line from the surface of an opaque ($A_V \sim 200^m$ in the center), spherical cloud. Thus $A_{V,1D}$ measures the amount of radiation reaching the grain (see Sect. 3.2 for more). Figure 1 shows a_{alg} as a function of $A_{V,1D}$ for four densities n_{H}.

Cho & Lazarian (2005) note that their goal is only to obtain a crude estimate. They make a couple of simplifications while deriving the above formula. First of all, they consider the anisotropy of the radiation only along the magnetic field, and neglect the isotropic radiation. They use the anisotropy factor $\gamma = 0.7$ for their dark cloud, in accordance with Draine and Weingartner (1996). Our model cloud, as will be shown later, is much different in structure, and has large volumes of optically thin medium, which are illuminated more or less isotropically. By using Eq. (1) in those regions, we overestimate the grain alignment efficiency. However, as our main goal is to examine the cores within the larger cloud, for which the anisotropy factor would be valid, we decide to use Eq. (1). We will return to
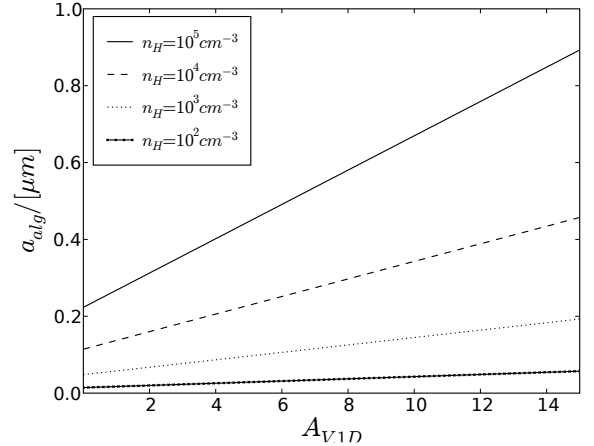

Fig. 1. Minimum aligned grain size as a function of $A_{V,1D}$ using the Weingartner & Draine (2001) dust model and Li & Draine (2001) grain size distribution.

the topic of anisotropy in Sect. 5.1. The relative attenuation of the radiation field at different wavelengths, and thus Eq. (1), depends on the grain size distribution. The study of those effects is beyond the scope of this paper, and Eq. (1) should be considered, as said before, just an approximation.

The polarization reduction factor is

$$R = \frac{\int_{a_{\text{alg}}}^{a_{\text{max}}} C_{\text{ran}} n(a) \, da}{\int_{a_{\text{min}}}^{a_{\text{max}}} C_{\text{ran}} n(a) \, da}, \tag{2}$$

where C_{ran} is the polarization cross section of a randomly aligned grain, $n(a)$ the grain number density, a the grain size, a_{min} the minimum size of the grains, a_{max} the maximum size, and a_{alg} the minimum aligned grain size.

2.2. Polarized thermal dust emission

The polarized thermal dust emission is calculated following the formalism in Fiege & Pudritz (2000). Self-absorption and scattering can be neglected at submillimeter wavelengths. The Stokes Q and U components are equal to the integrals

$$q = \int \alpha f \cos 2\psi \cos^2 \gamma \, ds, \tag{3}$$

$$u = \int \alpha f \sin 2\psi \cos^2 \gamma \, ds, \tag{4}$$

where α is a coefficient of the particle properties to be defined later, f a weighting function related to the intensity of the local dust emission, ψ the angle between the projection of $\boldsymbol{B}$ on the plane of the sky and the north, and γ the angle between the local $\boldsymbol{B}$ vector and the plane of the sky. In Padoan et al. (2001), the weighting function f was the local gas density ρ, while here we also consider the case where the weighting function is the true dust emission intensity at the given wavelength, obtained from the radiative transfer calculations.

The polarization angle χ is given by

$$\tan 2\chi = \frac{u}{q}, \tag{5}$$

and the degree of polarization P is

$$P = \frac{\sqrt{q^2 + u^2}}{\Sigma - \Sigma_2}, \tag{6}$$

with

$$\Sigma = \int f \, ds, \tag{7}$$

and

$$\Sigma_2 = \frac{1}{2} \int \alpha f \left(\cos^2 \gamma - \frac{2}{3} \right) ds. \tag{8}$$

The coefficient α is defined as

$$\alpha = RF \frac{C_{\text{pol}}}{C_{\text{ran}}}, \tag{9}$$

where R is the Rayleigh polarization reduction factor due to imperfect grain alignment, F is the polarization factor due to the turbulent component of the magnetic field, C_{pol} is the grain polarization cross section, and C_{ran} is the average cross section of a randomly aligned grain. For more details, see Lee & Draine (1985).

In our study, $F = 1$ because the three-dimensional magnetic field is given by the MHD models, and we assume that the small-scale structure is resolved in the numerical solution. The ratio $C_{\text{pol}}/C_{\text{ran}}$ needs to be fixed because we want to study the effects caused by variations of R. To avoid unreasonably high polarization degree, we choose $C_{\text{pol}}/C_{\text{ran}} = 0.15$. This corresponds to the axial ratio of roughly 1.1 (see Fig. 1 in Padoan et al. 2001). In our study, we use both uniform $R = 1$, as well as R, which varies according to the local efficiency of the radiative torque, as explained in Sect. 2.1.

3. Models

In this section, we describe the MHD models and the radiative transfer calculations that are used in the simulation of the dust polarization.

3.1. MHD models

In this work, we use the three numerical models – A, B, and C – which are described in detail in Juvela et al. (2001). They are based on the results of numerical simulations of highly supersonic magnetohydrodynamic turbulence, run on a 128^3 computational mesh with periodic boundary conditions. The initial density and magnetic field were uniform and an external random force was applied to drive the turbulence at roughly constant rms Mach number of the flow. All three models have highly supersonic flows with the rms sonic Mach number $M_s \sim 10$. Models B and C are super-Alfvénic, with $M_A \sim 10$, while model A has equipartition of magnetic and turbulent kinetic energy, $M_A \sim 1$, and thus an order of magnitude stronger magnetic field than the other two. Model C also includes the effect of self-gravity. Details of the numerical code used to solve the MHD equations can be found in Padoan & Nordlund (1999).

3.2. Radiative transfer calculations

In our scheme, radiative transfer calculations are needed for two purposes. First, the radiative transfer is solved to compute the dust temperature and the resulting emission, based on a Monte Carlo code discussed in detail elsewhere (Juvela & Padoan 2003; Juvela 2005). The total intensity of the dust emission is used later to analyze the P/I-relations. Once the total intensity and polarization are computed, radiative transfer effects can be ignored, because the dust emission is optically thin at the wavelengths

considered ($\lambda > 100 \, \mu$m). Second, the radiative transfer is also calculated to estimate the three-dimensional distribution of the radiation field inside the model clouds, which is needed to compute the minimum grain size for alignment. This simulation is done in the V-band (0.55 μm), and the computed ratios between the local and the background intensities, I/I_{bg}, are transformed into $A_{\text{V,eff}}$ according to the formula

$$I/I_{\text{bg}} = \exp(-1.086 \times A_{\text{V,eff}}). \tag{10}$$

The values of $A_{\text{V,eff}}$ are then used to estimate the minimum size of aligned grains according to Eq. (1). However, this $A_{\text{V,eff}}$ is not the same $A_{\text{V,1D}}$ as used by Cho & Lazarian (2005). $A_{\text{V,eff}}$ is a measure of the amount of external radiation reaching a grain (see Eq. (10)). In the center of a homogeneous and spherically symmetric cloud, $A_{\text{V,eff}}$ would be equal to $A_{\text{V,1D}}$ (half of the A_V through the whole cloud). In inhomogeneous clouds the radiation propagates preferentially along low A_V sight lines. Therefore, the value $A_{\text{V,eff}}$ can be significantly smaller than the average A_V that would be calculated as an arithmetic average over all directions. As $A_{\text{V,1D}}$ is calculated along the lowest A_V sight line (i.e., perpendicular to the surface), the actual amount of radiation reaching the cell is less than in the case where $A_{\text{V,eff}}$ would have the same numerical value. Thus, a given value of $A_{\text{V,eff}}$ needs to be transformed into a lower value of $A_{\text{V,1D}}$ to derive the same radiation field. This is done in our case by numerically integrating over all directions to derive the actual total radiation reaching the cell as a function of $A_{\text{V,1D}}$. This allows the matching of the corresponding values of $A_{\text{V,1D}}$ and $A_{\text{V,eff}}$.

In the calculations, the dust properties correspond to normal Milky Way dust with $R_V = 3.1$ (Weingartner & Draine 2001), and we use the scattering functions calculated by Draine (2003)[1]. The cloud models are scaled to a linear size $L = 6$ pc and a mean density $n = 640 \, \text{cm}^{-3}$. The radiative transfer calculations depend only on column density, which is $\langle N(H) \rangle = 1.2 \times 10^{22} \, \text{cm}^{-2}$, corresponding to $\langle A_V \rangle \sim 6^{\text{m}}$. However, the absolute gas density enters the calculations through the density dependent polarization reduction factor R (see next section).

4. Results

4.1. Polarization maps

We calculate R in the following manner. First, we transform $A_{\text{V,eff}}$ to the corresponding $A_{\text{V,1D}}$ and use $A_{\text{V,1D}}$ to calculate a_{alg} from Eq. (1) for each cell. We set $a_{\text{min}} = 0.005 \, \mu$m. We use two power-law distributions, $n(a) \propto a^{-3.5}$, with sharp cut-offs at $a_{\text{max}} = 0.25 \, \mu$m and $a_{\text{max}} = 1.0 \, \mu$m. As a third grain size distribution, we also use the model of Li and Draine (2001), hereafter L&D, which is not a pure power law and has an effective cut-off between the previous a_{max} limits. Equation (2) is solved numerically to obtain the values of the resulting polarization reduction factors for a grid of values of n_H and $A_{\text{V,1D}}$. In the actual cloud model, the R-values are obtained for each cell by interpolating from the pre-calculated grid, rather than by solving Eq. (2) for each cell separately. The polarization reduction factor R as a function of $A_{\text{V,1D}}$ is shown in Fig. 2 for the different grain size distributions and different densities. As the maximum grain size increases, the R factor becomes less dependent on both the density and the value of the extinction, $A_{\text{V,1D}}$. This is the direct consequence of Eq. (2), as a_{alg} reaches a_{max} less rapidly.

---

[1] The dust optical properties are available on the web at
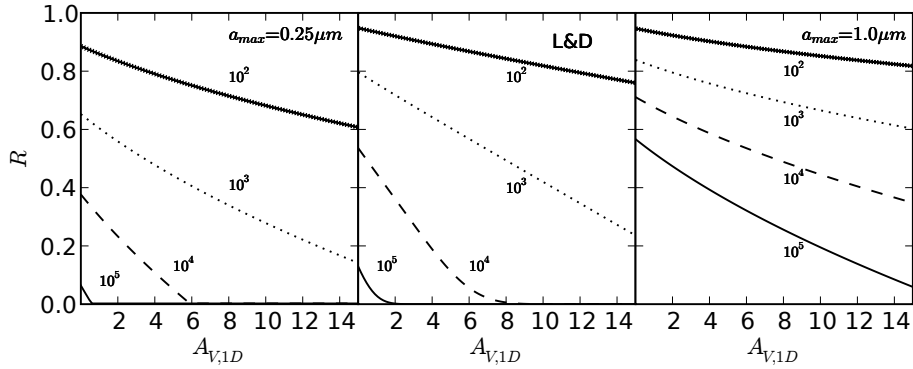www.astro.princeton.edu/~draine

Fig. 2. Polarization reduction factor R as a function of $A_{V,1D}$ using Weingartner & Draine (2001) dust model. The curves correspond to different densities. The frames correspond to different values of the maximum grain size, a_{max}. In the *first* and the *third frame* the grain size distributions are pure power laws, $n(a) \sim a^{-3.5}$, while in the *middle frame* the size distribution is taken from Li & Draine (2001).
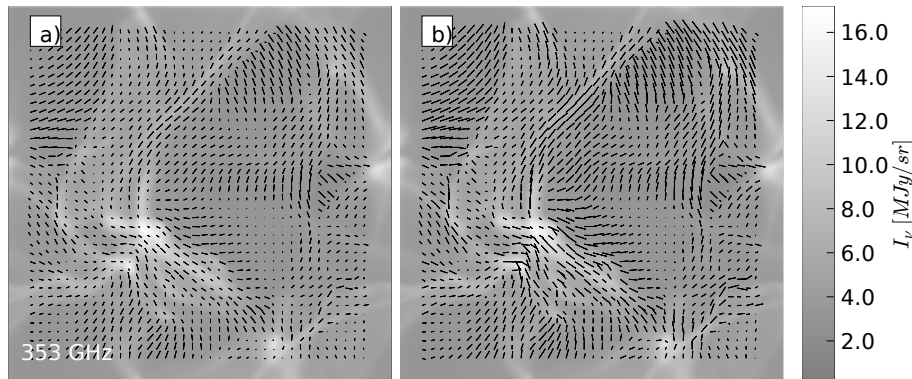

Fig. 3. Simulated polarization maps at 353 GHz with variable R (*left frame*) and uniform $R = 1$ (*right frame*). Polarization vectors are drawn for every third pixel, and the scaling of the vector lengths is the same in both frames. In the left frame the maximum polarization degree is 9%, while in the right frame it is 13%. The background image shows the total intensity at this frequency.

In the calculations of the polarization maps, we use model C as our baseline, which is scaled to the size $L = 6$ pc and mean density $n = 640$ cm^{-3}. This results in an optically thick cloud with average visual extinction $\langle A_V \rangle \sim 6.3^m$ through the cloud. We also choose 353 GHz as our base frequency. Other frequencies and model clouds are examined later.

Figure 3 shows the calculated polarization maps for 353 GHz. The polarization is calculated using the actual three-dimensional distribution of dust emission, that is using the local dust emission at the given frequency as the weighting function f (see Eq. (3)). In the left frame the polarization reduction factor R varies according to the local values of density and $A_{V,1D}$, as shown in the middle frame of Fig. 2. In the right-hand frame a uniform value of $R = 1$ was assumed. The difference in the polarization degrees is clearly visible. In particular, with variable R the polarization degree decreases in regions of high intensity, while no such trend exists in the right-hand frame.

In Fig. 4 the polarization degree and intensities are shown for the whole maps. The shapes of the plots are quite similar for the two lowermost frames, which are for model C with constant and variable R factors. The wide range of polarization degrees at any given intensity is caused by the geometry of the magnetic field and not by any numerical noise. This can be clearly seen when comparing the results with the uppermost frame, which is for model A. Model A has a strong, structured magnetic field in the z-direction, with only small deviations. Thus, the depolarization effects of tangled magnetic fields in the line of sight are small, leading to a much tighter relation between P and I.
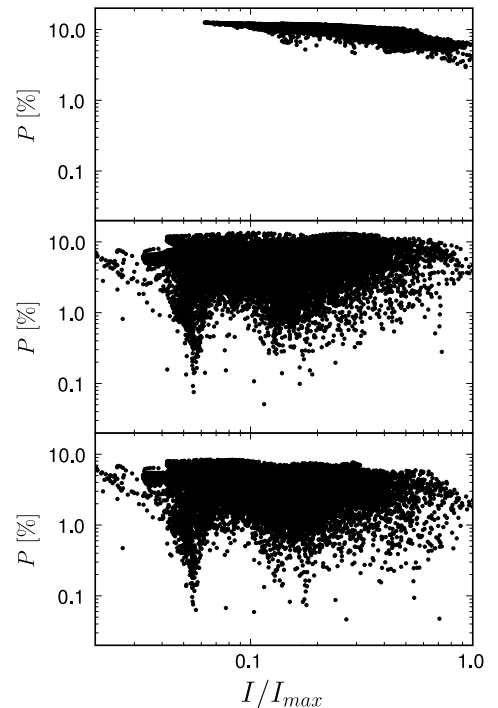

Fig. 4. Polarization degree for the whole 128^2 pixel maps, viewed from the y-direction. The *uppermost frame* corresponds to model A where the variable R factors are calculated using Li & Draine (2001) grain size distribution. The other frames are for model C with uniform $R = 1$ (*middle frame*) and variable R (*lower frame*), respectively.
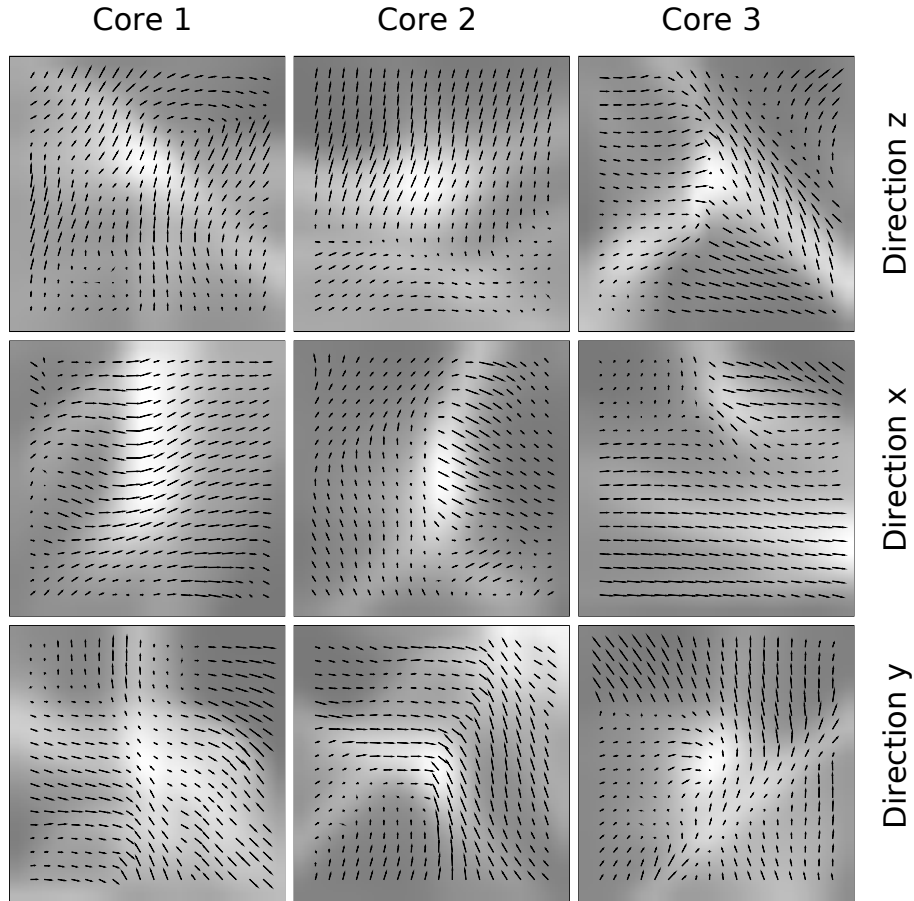
Fig. 5. Selected cores of model *C* observed at 353 GHz. The background grayscale map shows the intensity, and the vectors the direction and degree of polarization for the case of $R = 1$.

On a closer look, the two lowermost frames in Fig. 4 show some clear differences. First, there is a reduction of the maximum polarization degree from 13% to 9%. This is easily explained if one looks at the middle frame of Fig. 2 and recalls that we are considering a quite dense cloud, leading to $R < 1$ even in the low-density parts of the cloud. The low-intensity points to the extreme left are unaffected, but otherwise the polarization degree is clearly reduced, even for low intensity sight lines.

Another noticeable feature is the change in the upper envelope of the polarization degree. This can be seen by comparing the lower frames. With variable R, on sight lines with higher intensity (and higher average volume density), the maximum polarization degree becomes gradually smaller. In model *C* the effect is clear, but still small compared with the overall scatter in the polarization degrees. The overall slope is seen more clearly in the case of model *A* (the uppermost frame) because of the smaller scatter. The maximum polarization drops from about 12% to 6% in the interval $0.06 < I/I_{max} < 1.0$. These effects will be discussed further in the next subsection.

4.2. Self-gravitating cores

Figures 5 and 6 show zoomed 20 pixel by 20 pixel maps of selected cores of model *C* clumps. Maps are shown for both $R = 1$ and variable R. The model *C* included the effect of self-gravity. However, what is interpreted as a core in observations need not be a clear-cut, compact gravity-bound cores in reality. The same applies to these objects that were selected based on observations in the *y* direction. These are knots in the

filamentary cloud structure, and in certain directions the structures can be very elongated.

The general trend towards smaller polarization degree in the cores is obvious. The relation between observed total intensity and polarization degree is, however, not always clear. Density enhancements close to cloud edges provide one exception. Because they are subjected to unattenuated external radiation fields, they can exhibit large emissions although they have relatively low density compared with actual cores. Thus, the factor R is larger than in the cores and the polarization is very similar to that in the case of uniform R. One example of this can be seen in Core 3, when Figs. 5 and 6 are compared. This is particularly striking in the *x* direction, where the actual core is situated in an area of lower brightness slightly above the map center, while a bright filament on the cloud surface crosses the lower part of the map. Another thing to note is that the reduction of the polarization in the dense parts of the cloud can, in special cases, actually increase the total polarization degree. Core 2 provides an example of this, when observed from the *x*-direction. Although the polarization decreases in the bright core itself, the polarization increases immediately to the left of it. This is, of course, due to the magnetic field geometry. If the magnetic field is predominantly in the opposite direction in high and low density regions on the line of sight, they depolarize the observed intensity. When the polarization reduction factor reduces the polarization in the dense region, the depolarization effect is reduced and the observed net polarization is correspondingly increased. This is another indication of the fact that it is difficult to interpret observations of polarization if not in a statistical sense.
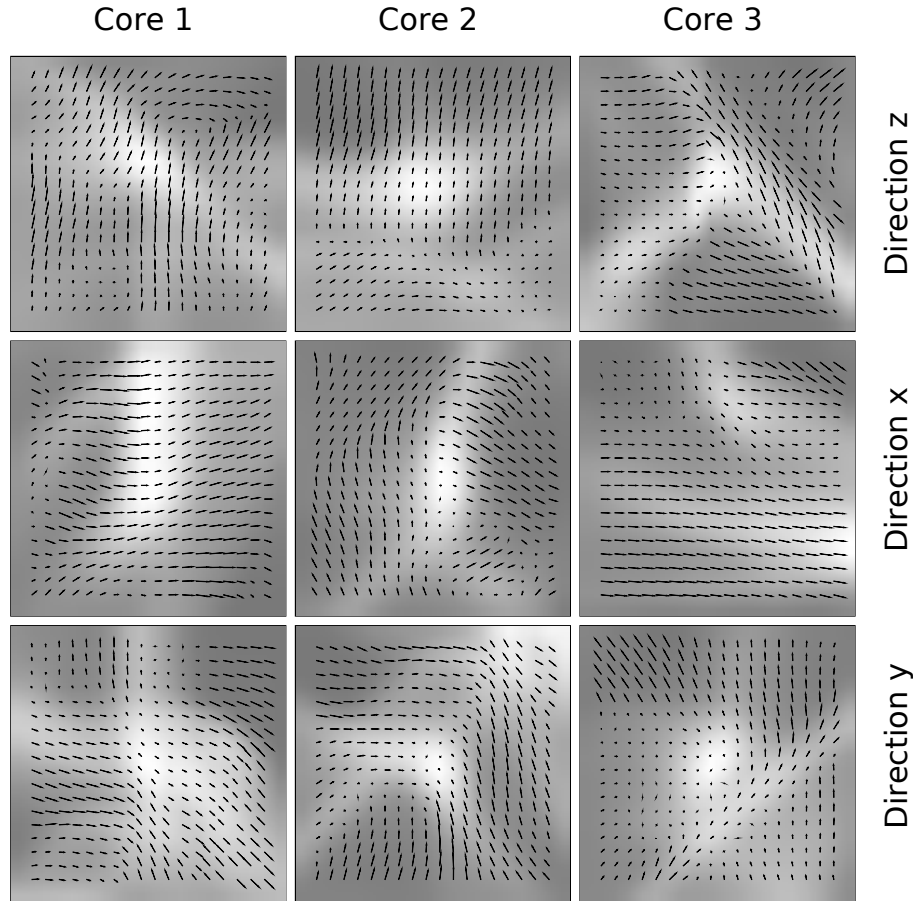
Core 1   Core 2   Core 3

Direction z

Direction x

Direction y

Fig. 6. Selected cores of model C at 353 GHz. The figure is identical with Fig. 5, but assumes variable polarization reduction factor, R.

Figure 7 shows the plotted P/I-relations for the cores seen in Fig. 6. In the x direction plot of Core 3, one can clearly identify the bright, high polarization filament on the edge of our cloud. Other bright but less dense (thus highly polarized) regions help to mask the slope. The observed polarization is a sum of many effects, depolarization being the most obvious one. For example, the large-scale structure of the cloud determines which parts of the cloud receive the most radiation from the external radiation field. This affects the efficiency of the radiative torque and of grain alignment (taken into account in $A_{V,1D}$ in Eq. (1)) and also heats up the dust grains, which increases their thermal emission. In the plots, the scaling of the x-axis depends on the maximum intensity, which, therefore, affects the appearance of the figures. One example of this is Core 2 seen in the y direction, where one can easily see the bright upper right corner of Fig. 6 represented as the cluster of high polarization, high intensity points in Fig. 7. If this area were omitted, the drop of polarization degree with intensity would become much more dramatic.

In Fig. 8 we look at some of these effects. In the uppermost frame we show the polarization degree in the z direction as a function of column density N for Core 2. The clump of low polarization points, identified with the filament in the lower portion of the image in Fig. 6, moves from moderate intensity to low column density. Thus these points are not part of any high-density core, and the low polarization is likely to be caused by the depolarization resulting from the magnetic field structure. If those points were omitted, we would end up with a quite clean P/I-relation for the core itself. Of course, the problem with this kind of approach is that, for an observer, the true column density is not known a priori. However, if accurate column density

estimates were made, this kind of point-to-point investigation would help in distinguishing between true cores and smaller density enhancements on the cloud surface. If the magnetic field is preferentially parallel to the filament, the result, high intensity and low polarization, mimics the appearance of a dense core with a small value of R. There are some examples of the opposite effect in the cores, where the fainter core points move to/towards the right in the plots when we shift from the intensity to the column density axis. Long filaments that are aligned along the line-of-sight would produce a relatively high surface brightness compared with the actual column density.

In the lowermost frame of Fig. 8, the difference between the uniform $R = 1$ case and the variable R depending on density and $A_{V,1D}$ is obvious. With $R = 1$ the maximum polarization increases, rather than decreases, to $\sim 10\%$ with increasing intensity. When R is variable there is a downward trend, ending at around 3% at the brightest regions. This is explained by the fact that intensity and density are usually connected. The high-intensity points correspond to the high column density. In the high density regions we also expect to find high $A_{V,1D}$. Thus, looking at the middle frame of Fig. 2, we see that the polarization reduction factor R decreases quite rapidly as we go to denser and more opaque regions. Therefore, those regions affect the polarization less, whereas in the $R = 1$ case, it is precisely the dense parts that contribute the most.

4.3. Effects of different cloud and dust models

In this section, we examine differences between different cloud models as well as discuss the possible effects of grain growth.
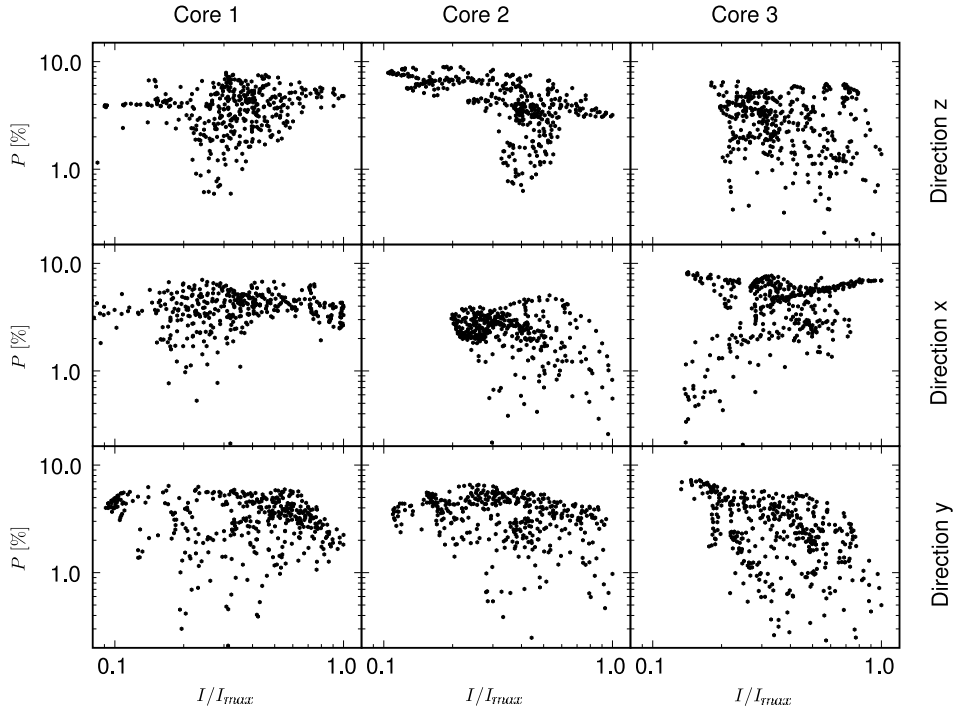
Fig. 7. The relation between polarization degree and total intensity for selected cores of the model C. The polarization degree has been calculated using the WD2001 dust model and variable polarization reduction factor, R.
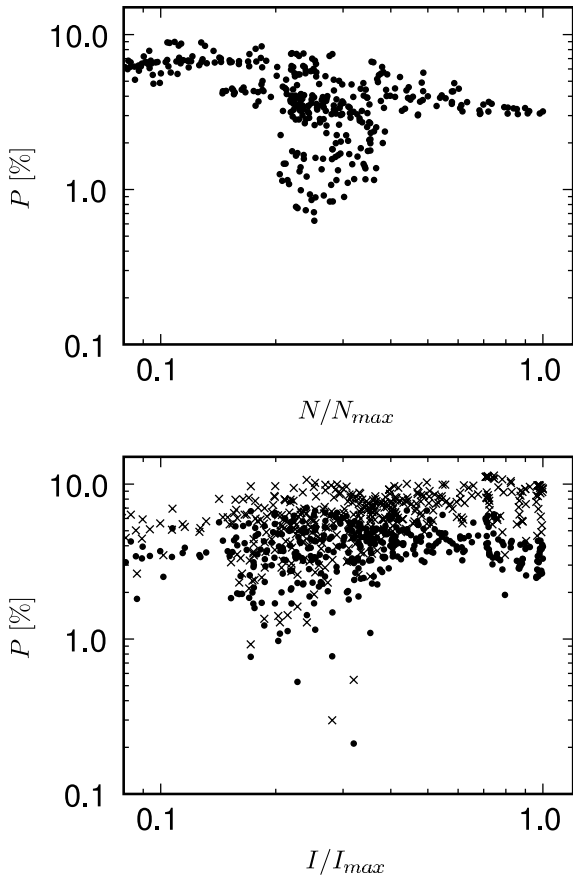

Fig. 8. Selected cases for comparison with Figs. 5 and 6. The *upper frame* shows the polarization degree for Core 2 as a function of true column density, when viewed from the z direction. The *lower frame* shows Core 1 viewed from the x direction, with variable R (dots) and uniform $R = 1$ (crosses). The polarization degree is plotted as a function of the total intensity at the same frequency of 353 GHz.

We will also briefly consider the effect of the choice of wavelength in our polarization calculation. Figure 9 shows some histograms for our three model clouds. Particularly noticeable is the sharp contrast when the polarization degree and angle of model A are compared with the other models B and C. Similarly, in model A there is a very strong dependence on the direction of observations. This results from the fact that model A has a very strong magnetic field that is aligned along the z-direction. There is little depolarization caused by magnetic field tangling, and, consequently, the polarization degree is high, and the angle of the polarization vectors is almost uniform. When model A is observed from the z-direction, the angle γ is close to perpendicular to the plane of the sky and hence $\cos^2 \gamma$ is small (see Sect. 2.2). Thus, the average polarized signal is small, and small variations in field geometry can lead to strong depolarization. However, because there is an obvious preferred angle even in the z-direction, we can say that the evolved magnetic field is not aligned perfectly along the z-axis, but has a small deviation from it.

Models B and C are both super-Alfvénic and, consequently, the field geometry is much more complicated. Comparing these two models, we notice that the polarization degree is slightly smaller in model C when observed from any direction. On the other hand, the distributions of polarization degrees are quite similar. While model C has slightly more very dense cores, probably due to its inclusion of self-gravity, the number of dense cells is so small that it seems implausible that R would be the cause of this difference, especially since model B shows a similarly large fraction of very dense cells. However, model B seems to have a slightly less tangled magnetic field and, therefore, less depolarization.

In Fig. 10 we show similar histograms for model C when the cloud is observed at resolutions corresponding to 1, 4, or 16 pixels. The four-pixel resolution seems almost identical to the original one. The 16-pixel resolution shows clear results of the averaging, by narrowing down the variance of the distributions. Of course, this is to be expected as soon as the beam size
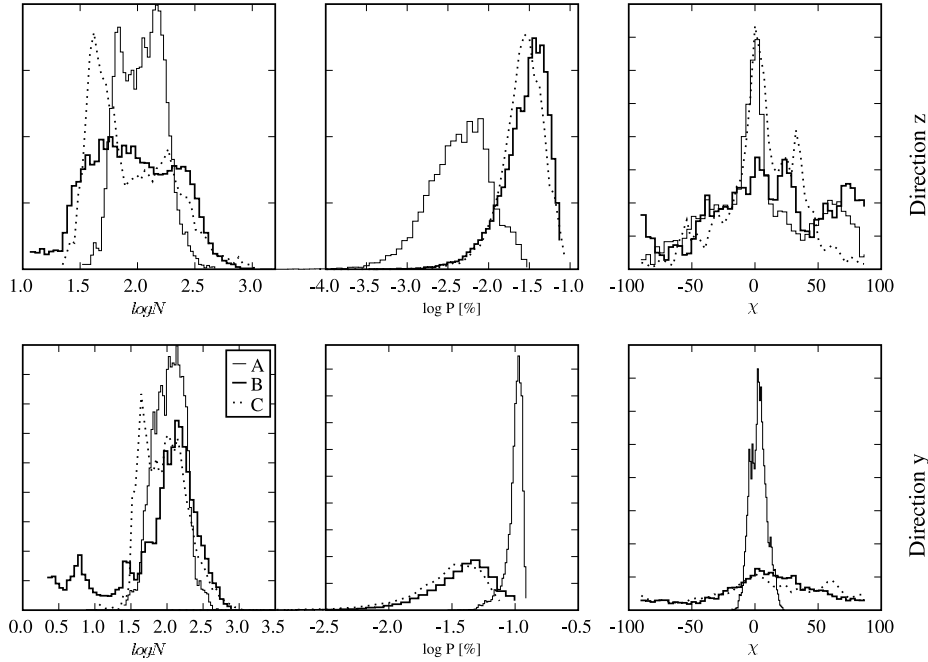
Fig. 9. Histograms of column density, polarization degree, and polarization angle for the three model clouds *A*, *B*, and *C*. The histograms of the polarization angle χ have been computed so that the maximum value is at zero angle.
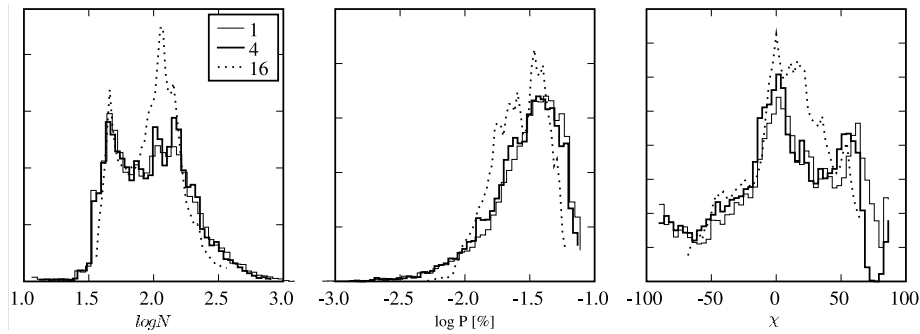

Fig. 10. Histograms of column density, polarization degree, and polarization angle computed for model *C* viewed from the *y*-direction. The three curves correspond to different resolutions of observation, corresponding to *FWHM* of either 1, 4, or 16 pixels.

exceeds the size of typical structures. If we are interested in the details, such as the cores, the best possible resolution is, of course, needed. On the other hand, for general morphological and statistical studies, the results are not very sensitive to a small reduction in resolution.

Figures 11 and 12 are similar to Figs. 6 and 7, showing Core 2 in the *y*-direction with the three different grain size distributions that were introduced at the beginning of Sect. 4.1. The increase of the polarization vectors and even a slight change of direction is clearly visible, as we move toward larger a_{max}. This can easily be explained by looking at Fig. 2. The smaller the parameter a_{max}, the faster R decreases as a function of density and $A_{V,1D}$. This is because in Eq. (2), a_{alg} quickly reaches the smallest a_{max}, while the largest a_{max} takes a larger range of $A_{V,1D}$ values to build up to, hence making the transition more smooth.

In Fig. 12 we see the drop in the maximum P, similar to the global plots. One can also see that while the two frames on the left resemble one another in shape, the rightmost frame is significantly different. This hints at the fact that at $a_{max} = 1$ μm, we are approaching the case of $R = 1$. This indicates that the number of very dense cells is relatively small, as can be seen from Fig. 9, and that $A_{V,1D}$ does not reach values as high A_V, the visual

extinction through the whole cloud. In an inhomogeneous cloud there are always low density regions and "holes" that allow external radiation fields to penetrate deep into the cloud. Therefore, $A_{V,1D}$ values can be much smaller than the average A_V, which, furthermore, is calculated through the whole cloud. In model *C*, $A_{V,1D}$ has a maximum value of 4.3^m and a mean value of 0.03^m. We can also see the slope of the decrease of maximum P slowly leveling off as we move to higher values of a_{max}.

In Fig. 13 we have calculated the polarization for Core 2 under different assumptions. In the first frame we use the Padoan et al. (2001) approach, and assume that the dust emission is directly proportional to the density. In practice, this means that the weighting function f in Eq. (3) is simply the local density. As a further consequence, the selected frequency has no effect on the polarization and affects only the intensity. The other two plots are calculated by taking into account the actual three-dimensional distribution of dust emission, i.e., the weighting function f is the local emission at the frequency in question. On the other hand, in these plots the polarization reduction factor R was assumed to be constant, $R = 1$. There is a clear, systematic change whereby the dynamic scale of the intensity axis becomes more narrow. The overall shape of the figures remains rather
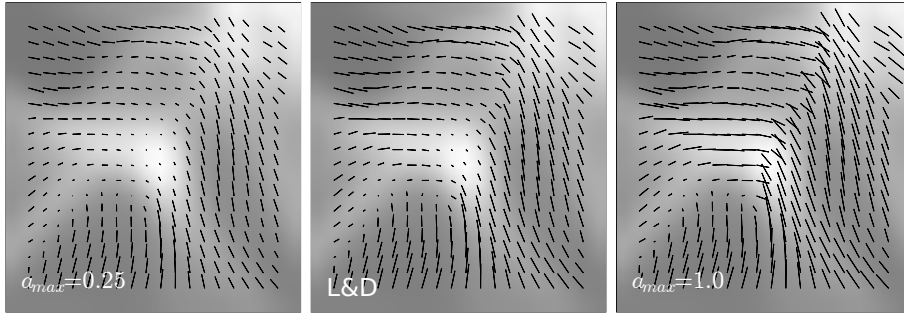
Fig. 11. Polarization observed toward Core 2 in the case of different values of a_{max}. The observations are made toward the y-direction. Polarization vectors are drawn for every pixel, and the scaling of the vectors is identical in all frames. The maximum polarization is 5.1% in the *left frame*, 6.6% in the *middle frame* and 7.8% in the *right frame*.
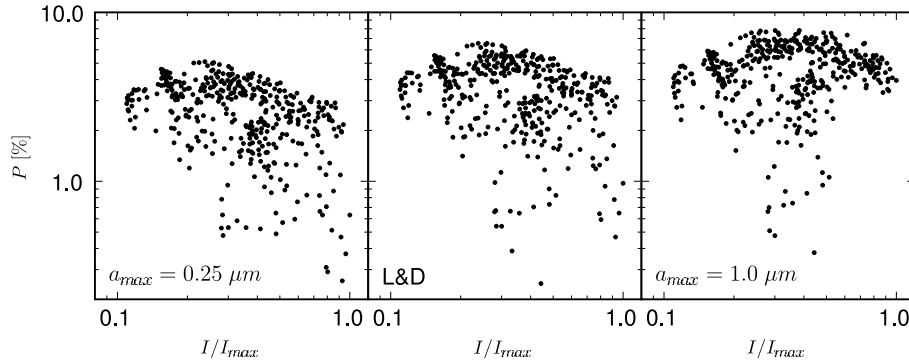

Fig. 12. Polarization degree as a function of intensity for Core 2 viewed from the y-direction. The frames correspond to different values of the maximum grain size, a_{max}. In the *first* and the *third frame* the grain size distributions are pure power laws, $n(a) \sim a^{-3.5}$, while in the *middle frame* the size distribution is taken from Li & Draine (2001).
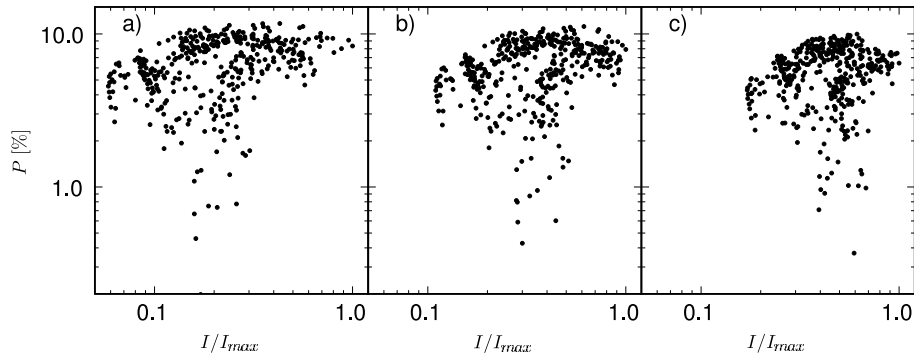

Fig. 13. Polarization degree of Core 2 viewed from the y-direction. The size distribution of the grains is taken from Li & Draine (2001). In the *first frame* the emission is assumed to be directly proportional to the local gas density, while in the *second frame* the actual calculated dust emission is used. These plots correspond to the frequency of 353 GHz (850 μm). In the *third frame*, the true three-dimensional distribution of dust emission is also used, but the calculations are done for 1500 GHz (200 μm). In all cases a uniform value of $R = 1$ was assumed.

similar, and there is only a small reduction in the expected polarization degree. The figures do, however, indicate that a change in the wavelength affects the relative weights that are given to different regions. When one moves to shorter wavelengths, the correlation between column density and observed intensity decreases. Optically thick regions contain cold dust and, therefore, radiate mainly at longer wavelengths. If one goes down to the far-infrared (~200 μm or below), the emission comes preferentially from optically thin regions and from the surface of optically thick cores and filaments. Therefore, shorter wavelengths work in a similar way to the variable polarization reduction factor, and the observed polarization map contains less and less information about magnetic fields inside the cores. Thus, the dense cores become indistinguishable from their surroundings.

4.4. Predictions for the Planck satellite

Planck[2] is a CMB mission of the European Space Agency (ESA) that is planned to be launched in 2007. The satellite will provide sensitive all-sky maps in a wide frequency range between 30 and 857 GHz. In the shortest wavelength channels, the Galactic dust emission will be the dominant emission component. Planck has polarization capabilities in seven channels (see Table 1). In the following we examine the observable dust polarization at two frequencies, 143 GHz and 353 GHz. We use monochromatic simulations and no convolution is done over the band profiles. However, the frequencies studied are relatively far in the Rayleigh-Jeans regime, so that this simplification is not expected

---

[2] http://www.rssd.esa.int/Planck/

Table 1. The performance goal values for the resolution and sensitivity of the Planck satellite. The expected sensitivities after 14 months of observations (two full-sky surveys) are given as thermodynamic temperature relative to the CMB temperature of 2.73 K. A more complete table is available through the ESA website `http://www.rssd.esa.int/?project=PLANCK&page=perf_top`

Center frequency (GHz)	Bandwidth (GHz)	Beamsize $FWHM$ (arcmin)	Sensitivity, I [$\Delta T/T \times 10^{-6}$]	Sensitivity, Q and U [$\Delta T/T \times 10^{-6}$]	Sensitivity, I [10^3 Jy/sr]	Sensitivity, Q and U [10^3 Jy/sr]
30	6	33	2	2.8	0.15	0.21
44	8.8	24	2.7	3.9	0.42	0.60
70	14	14	4.7	6.7	1.7	2.4
100	33	9.5	2.5	4.0	1.6	2.6
143	47	7.1	2.2	4.2	2.3	4.4
217	72	5	4.8	9.8	6.3	13
353	116	5	14.7	29.8	12	24
545	180	5	147	–	23	–
857	283	5	6700	–	26	–

to have a large effect, apart from a possible small error in the estimated absolute values of the intensities. Our previous tests already showed that morphological differences will arise only in comparison with much shorter wavelengths (see Fig. 13).

For this test we use model *C*. The model was previously scaled to represent a cloud with a size of 6 pc and mean density 640 cm^{-3}, resulting in an optically thick cloud with average visual extinction $\langle A_V \rangle \sim 6.3^m$. This was done to bring out the effects associated with high densities and high values of the effective extinction (e.g., in Eq. (1)). Here we want to study whether the polarized signal might still be detectable in regions of low column density. Therefore, we scale the column densities down by a factor of ten, resulting in a model with average extinction $\langle A_V \rangle \sim 0.6^m$. Simulations are done using a variable polarization reduction factor R that corresponds to the Weingartner & Draine (2001) dust model. Noise is added to the total intensity and the Q- and U-components according to the values given in Table 1.

Figure 14 shows the computed polarization map for 143 GHz. In the figure we have also plotted contours corresponding to A_V values of 0.5 and 2.5 mag. Below $A_V \sim 0.5$, the polarized signal is dominated by noise, which randomizes the angles and increases the average polarization degree. Only above $A_V \sim 2.5^m$ is the signal comparable to the noise. On the other hand, for total intensity the signal-to-noise ratio is high and the noise has no visible effect on that parameter. The average intensity over this map was 1.8×10^4 Jy/sr, while the $1 - \sigma$ noise, 2.3×10^3 Jy/sr, is smaller by about one order of magnitude.

In Fig. 15, a similar plot is shown for 353 GHz. In terms of absolute intensity, the sensitivity is lower at this frequency. However, the rise in the dust spectral energy distribution more than compensates this, and the signal-to-noise ratio is significantly higher. The polarization vectors follow, with some scatter, the magnetic fields even along filaments with $A_V \sim 1^m$ or more. At 353 GHz, the spatial resolution of Planck is 5 arcmin so that the pixel size is somewhat smaller than in Fig. 14.

The sensitivity can be increased by reducing the spatial resolution. In Fig. 16 the pixel size of the previous maps is set equal to 5 arcmin, and the maps have been convolved down to a resolution of $FWHM = 15$ arc minutes. The signal-to-noise ratio is, of course, correspondingly larger by a factor of ~3. At 353 GHz a comparison with Fig. 15a shows that the orientation of the polarization vectors is generally correct above $A_V \sim 1^m$, and is no longer completely random even in the regions with the lowest column density. At 143 GHz the scatter is larger, and thus even in the regions with $A_V \sim 2.5^m$ the true polarization field cannot be reliably measured. The errors of polarization degree P (solid line, left-hand scale) and polarization angle χ (dashed line,
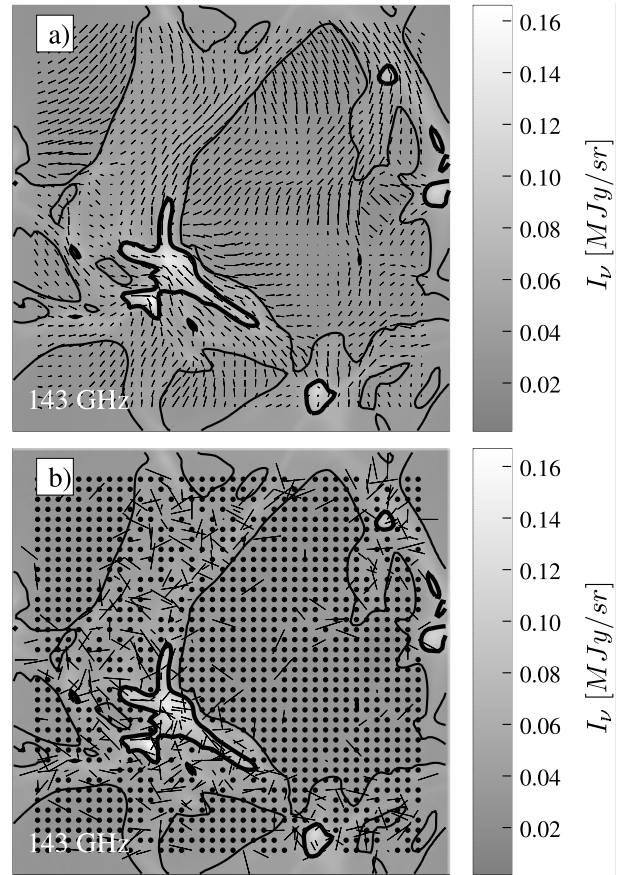

Fig. 14. Simulated polarization map at 143 GHz without noise (*upper frame*) and with noise corresponding to observations with the Planck satellite (*lower frame*). The cloud is model *C*, scaled down to $\langle A_V \rangle = 0.6^m$. One pixel corresponds to 7 arc minutes, the Planck resolution at this frequency. Polarization vectors have been drawn for every third pixel, and the scaling of the vectors is the same in both frames. In the upper frame the maximum polarization degree is 9%. In the bottom frame noise dominates and, for clarity, long vectors are cut at 25% and replaced by a dot. The background image shows the total intensity, and the contours denote A_V values of 0.5 and 2.5 mag.

right-hand scale) of the convolved 353 GHz map are shown in Fig. 17. At $A_V \sim 1^m$ the relative error of P is ~40% and of χ is ~30 degrees. At $A_V \sim 2^m$ the errors are already relatively low, ~25% for P and ~15 degrees for χ.

The 143 GHz band is already close to the peak of the CMB spectrum, but, even at these column densities, the total signal is dominated by the dust emission. In the previous 143 GHz map
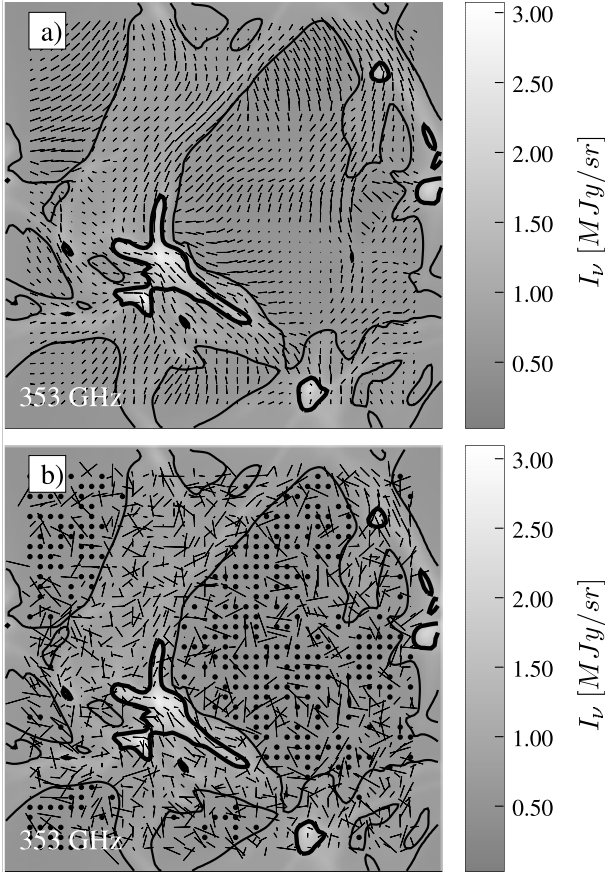
Fig. 15. Simulated polarization map at 353 GHz without noise (*upper frame*) and with noise corresponding to observations with the Planck satellite (*bottom frame*). Without noise the maximum polarization degree is 9%. In the upper frame map, long vectors are cut at 25% and replaced by a dot. One pixel corresponds to the Planck resolution of 5 arcmin. Polarization vectors are drawn for every third pixel along both axes.

Fig. 16. The effect of convolution on the polarization maps shown in Figs. 14 and 15. One pixel of the original simulation is assumed to correspond to 5 arcmin, and the maps are convolved down to a resolution of 15 arcmin.

the minimum column density is 1.1×10^{20} cm^{-3}, corresponding to less than 0.1 mag of visual extinction and a surface brightness of $\sim 3 \times 10^3$ Jy/sr. At this frequency, the intensity of the CMB signal, 3.8×10^2 Jy/sr, is still lower by almost one order of magnitude. Because the polarization degree is of the same order for both the dust emission and the CMB, the polarized signal will also be dominated by the dust emission. Conversely, the CMB signal introduces errors to the estimated dust polarization signal only at the 10% level. If one wishes to study the dust emission at any fainter level, the CMB should be taken into account as a possible error source. Of course, at higher frequencies the contribution of the CMB signal becomes negligible, and the combination of several wavelengths makes dust polarization studies possible even at fainter levels, if the resolution is correspondingly decreased. Conversely, in Planck CMB observations, the dust contamination is minimized by using measurements at high galactic latitudes and lower frequency bands, 70 GHz and 100 GHz.

5. Discussion

5.1. Current polarization model

We have shown dust polarization maps computed for model clouds that are based on three-dimensional MHD simulations. The main improvement with respect to the previous study by Padoan et al. (2001) is that we have calculated the true
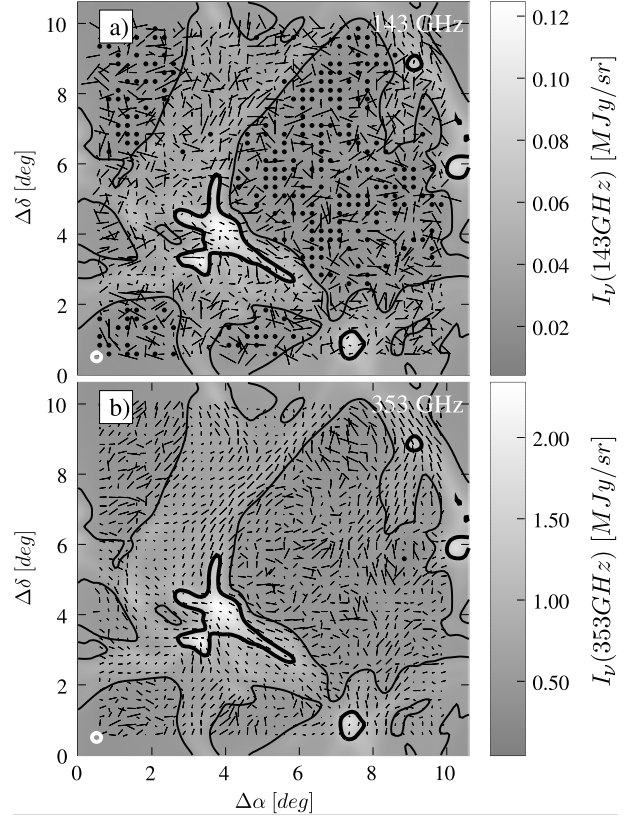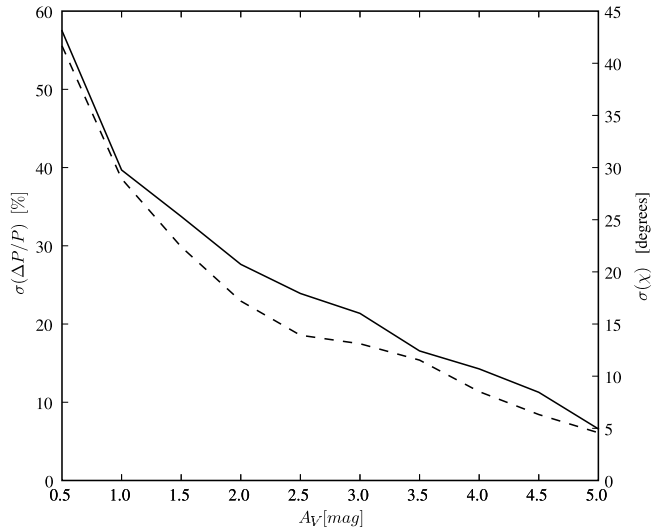

Fig. 17. The errors of polarization degree P (solid line, left-hand scale) and polarization angle χ (dashed line, right-hand scale) of the convolved 353 GHz map in Fig. 16.

distribution of dust emission with the aid of three-dimensional radiative transfer calculations. This affects the way different volume elements contribute to the observed signal. Furthermore, instead of resorting to an ad hoc model, the polarization reduction factor has been calculated according to the model of Cho & Lazarian (2005). In this model the grain alignment depends on radiative torques and, consequently, radiative transfer calculations have also been used to estimate the strength of the

external radiation field at each position of the model clouds. This has been accomplished through the determination of values of $A_{V,eff}$.

Observations show a decreasing polarization degree toward dense cores. Gonçalves et al. (2005) proposed a geometrical effect, the toroidal magnetic field lines bending to resist the gravitational pull, to partly explain this drop. Padoan et al. (2001) could explain the observed reduction by a qualitative model where the dust alignment was restricted to regions with A_V below 3^m. This extinction was calculated in a similar fashion to our $A_{V,eff}$. With our models we find a very similar behavior in the plots of polarization degree vs. intensity (e.g., Fig. 6). At low column densities the polarization degree varies between ~4 and 10% while, at the center of the cores, the degree drops to a few percent or, in some cases, even below one per cent. In other words, our physical model is capable of explaining the general observed behavior (e.g., Ward-Thompson et al. 2000; Henning et al. 2001). At the same time, the individual fields show considerable variations, and we also find cases with no apparent decrease in the polarization degree (e.g., Core 3 and z direction) or even increased polarization around intensity maximum (Core 3 and the filament seen toward x direction). This indicates that observations of individual cores may show considerable variation, depending on the actual configuration of the magnetic field. One apparent problem is that from observations it may be difficult to discern real and possibly gravitationally bound cores from projection effects. In particular, a core with a large polarization reduction factor may appear very similar to a filament with a major axis and field lines parallel to the line of sight.

The individual contributions of local density and $A_{V,1D}$ to the reduction of the polarization degree also merit a mention. In model C the local density varied between ~1 and ~10^5 cm^{-3}, while $A_{V,1D}$ had values from 0.005 to 4.3. Just by looking at Eq. (1) it is easy to see that on a global scale, the variation in local density dominates over $A_{V,1D}$. However, in the cores, where the densities are around the same order of magnitude, the contribution of $A_{V,1D}$ comes to its own by emphasizing the difference between the illuminated regions on the outer parts of the core and the shadowed, even denser interior. In cores, both local density and $A_{V,1D}$ are of similar importance.

The isotropic and anisotropic components of the radiation field, which play a major part in the efficiency of grain alignment by radiative torques, are related to this issue. In this work, we neglected detailed simulation of the anisotropy of the radiation field needed to derive the actual values of the anisotropy factor, γ, and instead used the fitting formula (Eq. (1)) by Cho & Lazarian (2005), where $\gamma = 0.7$. Draine & Weingartner (1996) give $\gamma = 0.1$ for diffuse clouds, due to the anisotropy of the star distribution in the Galaxy. We can qualitatively estimate the effect that the change of γ would have as it would be similar to the increase of local density by the corresponding inverse factor. For example, the difference between 10^2 and 10^3 cm^{-3} at low $A_{V,1D}$ (see Fig. 2) is a drop from 0.95 to 0.8 in R. Thus, we would expect a slightly lower polarization in those regions, but not by much. If anything, it would help to reduce the "contamination" of the diffuse background and make the cores stand out more. Also, because we would expect to see a more isotropic field at the center of the core than at its exterior, the inclusion of γ would make the core centers drop in polarization even more sharply. In other words, our model is likely to overestimate the polarization at the core centers, rather than the opposite.

In the modeling we assumed dust properties to remain constant throughout the model clouds, while only the alignment of the grains was dependent on the local density and the visual extinction. However, there is ample evidence that optical dust properties do change already above a few magnitudes of A_V. If this were caused primarily by a change in grain size distribution, this could counteract the reduction obtained via the R factor. As an example, let us consider an optically thick core with density $n \sim 10^4$ cm^{-3} and $A_{V,1D} \sim 6^m$. According to Fig. 2 the R-factor could increase by several factors if the L&D grain distribution were replaced with a distribution with much larger a_{max}. On the other hand, Fig. 12 shows that, in the actual model, the effect of an increasing a_{max} was rather limited. In that particular case, when the L&D dust model is replaced with an MRN type distribution with $a_{max} \sim 1\mu m$, the polarization degree increases in the core center only from ~2% to ~3%. It is very unlikely that in such a core a_{max} could grow close to one micron. Another explanation for the relative insensitivity to a_{max} is that the observed intensity is weighted toward low density material. There are two reasons for this. First, the polarization reduction factor decreases rapidly, whatever the value of a_{max}. Second, in a dense core the dust is colder and, therefore, the emission is lower for a given column density. In a core with $A_{V,1D} \sim 7^m$ to the center, the dust temperature may already be reduced to ~14 K or below (Stamatellos & Whitworth 2003). This can be compared with ~18 K in diffuse material. In the Rayleigh-Jeans tail the effect is small, and even at 353 GHz it is only a factor of 1.5. However, the effect becomes important when one approaches the peak of dust emission. At 100 μm the intensity produced by an 18 K grain is already ten times as large as the intensity produced by a 14 K grain. From Fig. 2 one can see that at low densities the slope of the R vs. $A_{V,1D}$ relation is very similar for all values of a_{max}, and the percentile difference in the absolute value of R is similarly small.

The above picture may change if dust grains undergo more profound changes. The sub-mm emissivity of dust has been observed to increase significantly in clouds that already have a visual extinction of only a few magnitudes (Bernard et al. 1999; Stepnik et al. 2003). This has been interpreted as evidence of not only grain growth, but the appearance of dust aggregates and fluffy grains of low packing density. At long wavelengths the high emissivity might again increase the contribution that the densest regions have on the total intensity observed towards cores. On the other hand, the formation of dust aggregates can also affect the intrinsic polarization efficiency of the grains and change the efficiency of the alignment mechanisms (Lazarian & Efroimsky 1999; Gupta et al. 2006). Such effects are not considered in this paper.

5.2. Comparison with other simulations

On larger scales, Prunet et al. (1998) presented simulations of polarized dust emission at high Galactic latitudes. The calculations were based on three-dimensional cloud structure that was estimated based on HI data. The HI line velocity provided information on the line-of-sight density distribution. The simulations assumed constant dust properties with intrinsic polarization efficiency ~30%. Furthermore, three field geometries were considered. A uniform field direction resulted in high polarization degree with very narrow distribution, and was dismissed as being incompatible with observations. In our simulations this corresponds closely to model A, where the field lines have remained almost parallel because of the strength of the magnetic field. Of course, strong polarization also requires that the cloud is not observed parallel to the field lines. In our model A, when the sight lines were perpendicular to the field lines, the polarization degree peaked around 10%. For a random orientation the mean
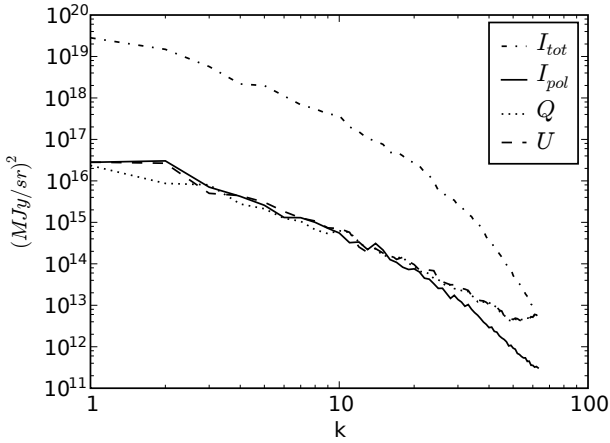
Fig. 18. The power spectra of the polarized intensity I_{pol} and the Stokes parameters I_{tot}, Q and U are plotted for model C from y direction. Column density N follows the intensity power spectrum closely, and is thus not shown. While model A showed a distinct shift in the level of the Q and U power spectrum in z direction, it – and model B – were not different enough in shape to justify another figure.

polarization would be lower by half. In the other two cases studied by Prunet et al., the field was assumed to be either parallel with the major axis of the cloud structures, or to have a random orientation perpendicular to it. Both resulted in a wider distribution of polarization degrees that, in the case of $R = 1$, peaked around 2–3%. These are again similar to our models B and C, where, irrespective of the viewing angle, we have an approximately log-normal distribution of polarization degrees that peaks around the value of ~3%. Therefore, although the results were obtained by entirely different methods, the basic properties of the dust polarization seem very similar. This is reassuring for attempts to build statistically meaningful all-sky templates for the polarized dust emission that will be observed, e.g., by the Planck satellite.

Another important statistic is the power spectrum of the polarized signal. Figure 18 shows the power spectra computed for the model C. Spectra are shown separately for the I, Q, and U components, as well as the polarized intensity I_{pol}, from y direction. These can be compared with the power spectra presented by Prunet et al. (1998). The slope of intensity, in interval $2 \leq k \leq 20$, is about k^{-3}, in agreement with Prunet et al. (1998). The Stokes parameters Q and U have a slightly more shallow slopes, but not as flat as those determined by Prunet et al. (1998). It can also be seen that in small scales, the power in the polarized components drops slower than the total intensity, making the polarized power an appreciable fraction of the total intensity power. The reason for this would appear to be the magnetic field morphology causing abrupt, pixel-to-pixel variations or larger structures, to about a 10-pixel level, while the background intensity stays about the same.

5.3. Comparison with observations

Direct observations of polarized dust emission are still very scarce for all but the very densest regions. The first detection of diffuse polarized dust emission was reported by Benoît et al. (2004). The observations were done with the balloon-borne Archeops experiment, with instruments that closely resemble those of the Planck satellite. Polarized signals could be detected at 353 GHz with the resolution of 13 arcmin, the average polarization degree being of the order of 4–5%. However, a large

variation was seen between different regions. In the Cygnus region the polarization was low, as can be expected if the magnetic field is preferentially parallel to the spiral arms. On the other hand, in some regions of the Galactic plane the polarization reached values of ~15%. In our models, polarization degrees this high could be reached only in model A and only when the polarization reduction degree R was equal to one (see Fig. 4). However, our maximum polarization degree is somewhat arbitrarily set by our choice of α, or to be more exact, our choice of $C_{pol}/C_{ran} = 0.15$. This ratio scales our maximum polarization degree to about 15.3%, which explains why we do not reach $P = 15\%$ in all our models, since that would demand a total alignment and no depolarization on the line of sight. A slightly larger, yet still moderate deviation from sphericity can double our polarization degrees: at an axial ratio of 1.2, $C_{pol}/C_{ran} = 0.3$. Thus one needs to be very careful not to overstate the case. Certainly a high polarization degree hints at an ordered magnetic field and high polarization efficiency throughout the cloud, yet even small changes in our assumptions about the grain shapes or lowering the density of our very dense model clouds would change the maximum polarization degree so that the other two models could duplicate even the high polarization degree of 15%.

Ponthieu et al. (2005) presented the measurements of temperature and angular power spectra of the diffuse emission of Galactic dust at 353 GHz as seen by Archeops on 20% of the sky. They concluded that if the fraction of the sky observed by Archeops is representative, dust polarized radiation will be a major foreground for determining the polarization power spectra of the CMB at high frequencies above 100 GHz. However, their power spectra cannot be directly compared with our results because they cover a much larger area, where the turbulence is no longer the dominant factor affecting the structure of the density and the magnetic fields.

5.4. Future

In Fig. 16 it is shown that when the spatial resolution of the Planck satellite is reduced to 15 arcmin, it will be able to provide a relatively clean map of the polarization of a diffuse cloud at 353 GHz. The general morphology of the magnetic field is more or less correct above $A_V \sim 0.5^m$, even if the polarization degree P itself has a relative error of ~60%, as seen in Fig. 17. The situation improves with increasing A_V, until at $A_V \sim 2^m$, the errors have dropped to the relatively low values of ~25% for P and ~15 degrees for the polarization angle χ. Thus, we conclude that Planck will be able to trace the general morphology of the magnetic fields at $A_V \sim 1^m$ and to map dust polarization reliably when A_V exceeds ~2^m.

In this study we have used simulations with relatively low spatial resolution. The results remain reliable at large scales, and the discussion of core properties is appropriate for general density enhancements and the initial phases in the formation of gravitationally bound cores. In a rotating and collapsing core the magnetic field lines become wound so that both the field strength and the depolarization caused by the field geometry increase. If the system were not perfectly symmetric one might, at high resolution, detect sharp variation in both the strength and direction of the polarization vectors. However, to be able to follow the development of magnetic fields inside such collapsing objects, simulations with considerably higher spatial resolution are needed. Spatially variable γ and the inclusion of other grain alignment mechanisms would allow a more realistic polarization model.

The work presented in this paper will be continued with such more detailed studies.

References

Abbas, M. M., Craven, P. D., Spann, J. F., et al. 2004, ApJ, 614, 781
Benoît, A., Ade, P., Amblard, A., et al. 2004, A&A, 424, 571
Bernard, J. P., Abergel, A., Ristorcelli, I., et al. 1999, A&A, 347, 640
Gonçalves, J., Galli, D., & Walmsley, M. 2005, A&A, 430, 979
Cho, J., & Lazarian, A. 2005, ApJ, 631, 361
Davis, L., & Greenstein, J. L. 1951, ApJ, 461, 909
Dolginov, A. Z. 1972, Ap&SS, 18, 337
Dolginov, A. Z., & Mytrophanov, I. G. 1976, Ap&SS, 43, 291
Draine, B. T. 2003, ApJ, 598, 1017
Draine, B. T., & Weingartner, J. 1996, ApJ, 470, 551
Fiege, J. D., & Pudritz, R. E. 2000, ApJ, 544, 830
Greenberg, J. M. 1968, in Nebulae and Interstellar Matter, ed. G. P. Kuiper, &
    B. M. Middlehurst (Chicago: Univ. Chicago Press), 7, 328
Gupta, R., Vaidya, D. B., Bobbie, J. S., & Chylek, P. 2006, Ap&SS, 301, 21
Hall, J. 1949, Science, 109, 166
Henning, T., Wolf, S., Launhardt, R., & Walters, R. 2001, ApJ, 561, 871
Hildebrand, R., Davidson, J. A., Dotson, J. L., et al. 2000, PASP, 112, 1215
Hiltner, W. 1949, Science, 109, 165
Jones, R. V., & Spitzer, L., Jr. 1967, ApJ, 147, 943
Juvela, M. 2005, A&A, 440, 531
Juvela, M., & Padoan, P. 2003, A&A, 397, 201
Juvela, M., Padoan, P., & Nordlund, Å. 2001, ApJ, 563, 853
Lazarian, A. 1994, MNRAS, 268, 713
Lazarian, A. 2003, J. Quant. Spectrosc. Radiat. Transfer, 79, 881
Lazarian, A., & Draine, B. T. 1999a, ApJ, 516, L37
Lazarian, A., & Draine, B. T. 1999b, ApJ, 520, L67
Lazarian, A., & Efroimsky, M. 1999, MNRAS, 303, 673
Lazarian, A., & Roberge, W. G. 1997, ApJ, 484, 230
Lazarian, A., Goodman, A. A., & Myers, P. C. 1997, ApJ, 490, 273
Lee, H., & Draine, B. T. 1985, ApJ, 290, 211
Li, A., & Draine, B. 2001, ApJ, 554, 778
Mathis, J. S., Mezger, P. G., & Panagia, N. 1983, A&A, 128, 212
Padoan, P., & Nordlund, Å. 1999, ApJ, 526, 279
Padoan, P., Goodman, A., Draine, B. T., et al. 2001, ApJ, 559, 1005
Ponthieu, N., Maćias-Pérez, J. F., Tristram, M., et al. 2005, A&A, 444, 327
Prunet, S., Sethi, S. K., Bouchet, F. R., & Miville-Deschênes, M.-A. 1998, A&A,
    339, 187
Purcell, E. M. 1979, ApJ, 231, 404
Stamatellos, D., & Whitworth, A. P. 2003, A&A, 407, 941
Stepnik, B., Abergel, A., Bernard, J.-P., et al. 2003, A&A, 398, 551
Ward-Thompson, D., Kirk, J. M., Crutcher, R. M., et al. 2000, ApJ, 537, L135
Weingartner, J. C., & Draine, B. T. 2001, ApJ, 548, 296